

Efficient and stable Ruddlesden–Popper perovskite solar cell with tailored interlayer molecular interaction

Hui Ren^{1,9}, Shidong Yu^{2,9}, Lingfeng Chao^{1,9}, Yingdong Xia¹, Yuanhui Sun², Shouwei Zuo³, Fan Li³, Tingting Niu¹, Yingguo Yang⁴, Huanxin Ju⁵, Bixin Li⁶, Haiyan Du¹, Xingyu Gao⁴, Jing Zhang³, Jianpu Wang¹, Lijun Zhang^{2*}, Yonghua Chen^{1*} and Wei Huang^{1,7,8*}

Two-dimensional Ruddlesden–Popper phase (2DRP) perovskites are known to exhibit improved photostability and environmental stability compared with their three-dimensional (3D) counterparts. However, fundamental questions remain over the interaction between the bulky alkylammoniums and the 2DRP perovskite framework. Here, we unambiguously demonstrate that a sulfur–sulfur interaction is present for a new bulky alkylammonium, 2-(methylthio)ethylamine hydrochloride (MTEACI). In addition to a weaker van der Waals interaction, the interaction between sulfur atoms in two MTEA molecules enables a (MTEA)₂(MA)₄Pb₅I₁₆ ($n=5$) perovskite framework with enhanced charge transport and stabilization. The result is 2DRP perovskite solar cells with significantly improved efficiency and stability. Cells with a power conversion efficiency as high as 18.06% (17.8% certified) are achieved, along with moisture tolerance for up to 1,512 h (under 70% humidity conditions), thermal stability for 375 h (at 85 °C) and stability under continuous light stress (85% of the initial efficiency retained over 1,000 h of operation at the maximum power point).

Two-dimensional Ruddlesden–Popper (2DRP) perovskites have attracted much attention for use in perovskite solar cells (PSCs) due to their improved moisture resistance¹, greatly enhanced photostability and thermal stability², ultralow self-doping (preventing unintentional defects³) and significantly reduced ion mobility⁴ in comparison to their traditional three-dimensional (3D) counterparts. 2DRP halide perovskites have the general chemical formula (RNH₃)₂A_{*n*-1}M_{*n*}X_{3*n*+1} (ref. ⁵), where RNH₃ represents bulkier organic ammonium, A, M and X are a small organic or alkaline metal cation, a group IVA metal and a halogen, as in 3D perovskites AMX₃, and *n* is an integer. The structure of a 2DRP perovskite can be envisaged as being ‘cut’ from a 3D perovskite along <100> crystal faces, forming a segment of the corner-sharing octahedral MX₆ layer⁶. The 2D layered segments are separated and bound together by the bulky ammonium bilayers that are alternately inserted as ligands to replace the original A-site cations. The Coulombic and hydrogen bonds between the organic and inorganic layers maintain the structural integrity⁷.

Substantial efforts have been devoted to improving the efficiencies of 2DRP PSCs^{8–12}. By aligning perovskite layers grown vertically onto a substrate with a hot-casting method, the power conversion efficiency (PCE) of a 2DRP PSC was boosted to over 12% (ref. ⁸) as a result of the facilitated charge transport. Further improved PCEs of 14.4% (ref. ⁹), 15.4% (ref. ¹⁰) and ~18% (refs. ^{11,12}) were recently

achieved by creating a narrower distribution of quantum well widths and by introducing additive-assisted film formation, controlling film growth and employing a vacuum poling technique. However, in spite of this progress, further improvements in efficiency as well as improved stability are needed to make 2DRP PSCs competitive with 3D PSCs for practical applications.

Compared with 3D perovskites, 2DRP perovskites have a unique degree of freedom that can be exploited to improve PSC efficiency—the bulky ammonium RNH₃ layer. This layer affects the intrinsic properties of 2DRP perovskites in several ways. (1) It truncates the 3D perovskite and provides a lower dielectric constant layer around the inorganic M–X sheets, giving rise to quantum confinement and dielectric confinement and thus promoting a large exciton binding energy^{12–16}. (2) It interacts electrostatically with the inorganic M–X sheets, which causes distortion of the perovskite framework and affects the electronic structure of the 2DRP perovskites^{17–20}. (3) It affects the crystal growth dynamics and thus the morphology/quality of the perovskite films¹¹. In recent years, numerous bulky ammoniums, such as phenylethylamine (PEA)²¹, butylamine (BA)²², polyethylenimine (PEI)²³, allylammonium (ALA)⁹ and 2-thiophenemethylammonium (ThMA)¹⁰, have been explored to continuously enhance the efficiency of 2DRP PSCs. However, one important effect related to the bulky ammonium layer—the interlayer interaction among adjacent 2DRP perovskite sheets—has rarely been

¹Key Laboratory of Flexible Electronics (KLOFE) & Institution of Advanced Materials (IAM), Jiangsu National Synergetic Innovation Center for Advanced Materials (SICAM), Nanjing Tech University (NanjingTech), Nanjing, Jiangsu, China. ²State Key Laboratory of Integrated Optoelectronics, Key Laboratory of Automobile Materials of MOE, and School of Materials Science, Jilin University, Changchun, China. ³Beijing Synchrotron Radiation Facility, Institute of High Energy Physics, Chinese Academy of Sciences, Beijing, China. ⁴Shanghai Synchrotron Radiation Facility, Shanghai Institute of Applied Physics, Chinese Academy of Sciences, Shanghai, China. ⁵National Synchrotron Radiation Laboratory and Collaborative Innovation Center of Suzhou Nano Science and Technology, University of Science and Technology of China, Hefei, Anhui, China. ⁶Department of Educational Science, Laboratory of College Physics, Hunan First Normal University, Changsha, Hunan, China. ⁷Shaanxi Institute of Flexible Electronics (SIFE), Northwestern Polytechnical University (NPU), Xi’an, China. ⁸Key Laboratory for Organic Electronics & Information Displays (KLOEID), and Institute of Advanced Materials (IAM), Nanjing University of Posts and Telecommunications, Nanjing, China. ⁹These authors contributed equally: Hui Ren, Shidong Yu, Lingfeng Chao. *e-mail: lijun_zhang@jlu.edu.cn; iamyhchen@njtech.edu.cn; iamwhuang@njtech.edu.cn

investigated. The interlayer interaction is mediated by the intertwined bulky ammonium bilayers and manifests as weak van der Waals and hydrogen-bonding interactions (Fig. 1a). This interaction controls the assembly of 2DRP layered perovskite segments and the charge transport across the segments¹⁶. Investigations of this interaction are expected to enable enhancement of stability and the optoelectronic conversion efficiency of 2DRP perovskite films.

Here, we report a joint experimental–theoretical study on tailoring the interlayer molecular interaction among 2DRP layered perovskite segments and investigating its impact on the efficiency and stability of 2DRP PSCs. Using the alkylammonium 2-(methylthio)ethylamine hydrochloride (MTEACl) as the bulky ammonium, we found that the strengthened interlayer molecular interaction was mediated by the sulfur–sulfur (S–S) interaction. The S–S interaction among the MTEA tails was further evidenced by the enhanced interlayer binding energy and the charge density overlap obtained from first-principles density functional theory (DFT) calculations. The S–S interaction-induced interlayer interaction enabled smooth, dense and pinhole-free 2DRP perovskite films with a low trap state density and allowed an efficient charge transfer process. Moreover, the MTEA-based 2DRP perovskite ($n=5$) films exhibited a strong out-of-plane preferential crystal growth with respect to the contacts over BA-based films. A high-performance 2DRP PSC with a PCE as high as 18.06% was achieved, surpassing the PCE of the BA-based device (15.94%). The strengthened interlayer molecular interaction significantly improved the environmental and thermal stability of the 2DRP perovskite films. Most importantly, the MTEA-based 2DRP PSCs still maintained over 85% of their initial efficiency under continuous light stress at the maximum power point (MPP) over 1,000 h.

Results and discussion

S–S interaction in $(\text{MTEA})_2(\text{MA})_{n-1}\text{Pb}_n\text{I}_{3n+1}$ 2DRP perovskites. The crystal structures of the studied MTEA-based 2DRP perovskites $(\text{MTEA})_2(\text{MA})_{n-1}\text{Pb}_n\text{I}_{3n+1}$ and, for comparison, BA-based counterparts $(\text{BA})_2(\text{MA})_{n-1}\text{Pb}_n\text{I}_{3n+1}$ are illustrated in Fig. 1a. These structures can be viewed as the 3D MAPbI_3 perovskite, truncated by the intertwined bulky ammonium layers of MTEA and BA, respectively. It should be noted that, because of the unavoidable formation of multiple 2DRP perovskite phases (with different n) of 2D perovskite layers during synthesis, the actual n value in this study is defined as the inorganic component number for the composition of PbI_2 , MTEACl or BACl, and MAI, with a stoichiometric molar ratio of $n:2:(n-1)$. For $(\text{BA})_2(\text{MA})_{n-1}\text{Pb}_n\text{I}_{3n+1}$ the interactions between the $-\text{CH}_2-$ tails of BA are weak van der Waals interactions. The involvement of the larger S atoms in the $-\text{CH}_2-$ tails of MTEA in $(\text{MTEA})_2(\text{MA})_{n-1}\text{Pb}_n\text{I}_{3n+1}$ creates a precondition for the formation of an extra chemical interaction between adjacent MTEA molecules. Indeed, we found a probable S–S interaction in the 2DRP $(\text{MTEA})_2(\text{MA})_4\text{Pb}_5\text{I}_{16}$ ($n=5$) perovskites via X-ray photoelectron spectroscopy (XPS). The $S(2p)$ spectra show one sulfur state with $S(2p_{3/2})$ and $S(2p_{1/2})$ binding energies of 162.8 and 164 eV, respectively, for the MTEA film (Fig. 1b). A shift to lower binding energy in the $S(2p)$ spectrum of the 2DRP $(\text{MTEA})_2(\text{MA})_4\text{Pb}_5\text{I}_{16}$ perovskites compared to that of MTEA can be observed for the two peaks associated with $S(2p_{3/2})$ and $S(2p_{1/2})$, from 162.8 and 164 eV to 162.2 and 163.4 eV, respectively (Fig. 1b). In contrast, no shifts in the $C(1s)$, $I(3d)$, $N(1s)$ and $Pb(4f)$ peaks are observed after carefully comparing the XPS spectra of 2DRP $(\text{MTEA})_2(\text{MA})_4\text{Pb}_5\text{I}_{16}$ perovskites with those of 3D MAPbI_3 perovskites (Supplementary Fig. 1). Because no interactions occur between S and other elements, for example, C, I, N and Pb, this shift may be caused by the S–S interaction between the $-\text{CH}_2-$ tails of MTEA in $(\text{MTEA})_2(\text{MA})_4\text{Pb}_5\text{I}_{16}$.

To further confirm our findings, we obtained X-ray absorption near edge structure (XANES) spectra of pure MTEA films and 2DRP $(\text{MTEA})_2(\text{MA})_4\text{Pb}_5\text{I}_{16}$ perovskite films. As shown in Fig. 1c, the

sulfur K-edge XANES spectra of MTEA and $(\text{MTEA})_2(\text{MA})_4\text{Pb}_5\text{I}_{16}$ are very similar, with the first sharp peak at 2,473.4 eV corresponding to the antibonding-type C–S bonds²⁴. The decrease of the peak intensity in the $(\text{MTEA})_2(\text{MA})_4\text{Pb}_5\text{I}_{16}$ perovskite films represents a change of the local charge distribution condition in proximity to the antibonding-type C–S bond compared with MTEA. This result indicates that the MTEA matrix (local electronic structure) is locally affected in the $(\text{MTEA})_2(\text{MA})_4\text{Pb}_5\text{I}_{16}$ perovskite, which may be due to the enhanced electron interaction between the S atoms in two MTEA molecules.

Having presented the experimental discovery of a probable S–S interaction, we aimed to further prove the S–S interaction in 2DRP $(\text{MTEA})_2(\text{MA})_{n-1}\text{Pb}_n\text{I}_{3n+1}$ perovskites through first-principles DFT-based energetic and electronic structure calculations. The $n=2$ case of $(\text{MTEA})_2\text{MAPb}_2\text{I}_7$ was chosen for simulation and compared with the counterpart $(\text{BA})_2\text{MAPb}_2\text{I}_7$. By optimizing the structures with different orientations of MA and MTEA/BA via total energy minimization, we identified the lowest-energy structures ($(\text{MTEA})_2\text{MAPb}_2\text{I}_7$ (i), upper panels of Fig. 1d and Supplementary Table 1). For $(\text{MTEA})_2\text{MAPb}_2\text{I}_7$, we observe a clear aggregation tendency of two S atoms from MTEA molecules belonging to different 2DRP layers. This phenomenon is distinct from the case of $(\text{BA})_2\text{MAPb}_2\text{I}_7$, where the $-\text{CH}_2-$ tails remain nearly upright, similar to the condition before 2DRP layers' stacking. The shortest distance between the S atoms of two MTEA molecules is 3.65 Å, reasonably falling in the range of the S–S interaction²⁵. The existence of the S–S interaction is further indicated by two aspects of the calculated results. (1) The interlayer binding energy of the stacked $(\text{MTEA})_2\text{MAPb}_2\text{I}_7$ layers with respect to the individual layers is 390 meV per f.u. (f.u., formula unit), much larger than the value of 90 meV per f.u. for $(\text{BA})_2\text{MAPb}_2\text{I}_7$. This result clearly suggests that the S–S interaction induces a strengthened interlayer molecular interaction in $(\text{MTEA})_2\text{MAPb}_2\text{I}_7$. (2) The electronic band structure of $(\text{MTEA})_2\text{MAPb}_2\text{I}_7$ (middle panel, Fig. 1d) shows S-derived states in proximity to the valence band edge. As shown in the upper and lower panels of Fig. 1d, the corresponding partial charge density (within the 1 eV window below the valence band maximum) has a large distribution in the interlayer region, and substantial charge density overlap occurs between two S atoms. This result is clearly in contrast to the case of $(\text{BA})_2\text{MAPb}_2\text{I}_7$, in which no corresponding visible charge density overlap is found in the interlayer region. Moreover, another metastable $(\text{MTEA})_2\text{MAPb}_2\text{I}_7$ structure with a 140 meV per f.u. higher energy ($(\text{MTEA})_2\text{MAPb}_2\text{I}_7$ (ii), Fig. 1d), which we obtained from structure optimization, shows S-derived states as valence band edges. The corresponding charge density also demonstrates an interlayer interaction mediated by the S–S interaction. To the best of our knowledge, the emergence of bulky ammonium-derived electronic states around the band edges has not been reported previously. These interlayer electronic states, which can be activated by temperature or impurity doping and can be transported across adjacent 2DRP layers, are expected to contribute to improved photo-induced charge carrier transport (as demonstrated in the following).

Highly oriented growth of $(\text{MTEA})_2(\text{MA})_{n-1}\text{Pb}_n\text{I}_{3n+1}$ 2DRP perovskites. The 2DRP $(\text{MTEA})_2(\text{MA})_{n-1}\text{Pb}_n\text{I}_{3n+1}$ family of perovskite compounds was prepared by deliberate control of the stoichiometry of PbI_2 , methylamine iodine (MAI) and MTEACl. From energy dispersive spectrometry (EDS) of $(\text{MTEA})_2(\text{MA})_4\text{Pb}_5\text{I}_{16}$ perovskite films (Supplementary Fig. 2), a well-distributed S element was observed, demonstrating the successful inclusion of MTEA in 2DRP perovskites. To assess the 2DRP perovskite morphology evolution with layer number n , we systematically investigated the morphology for different layer numbers from $n=1$ to 6 by scanning electron microscopy (SEM; Supplementary Fig. 3). A distinctive evolution of the thin-film surface is seen, where the 2DRP $(\text{MTEA})_2(\text{MA})_{n-1}\text{Pb}_n\text{I}_{3n+1}$ perovskite films exhibit platelet struc-

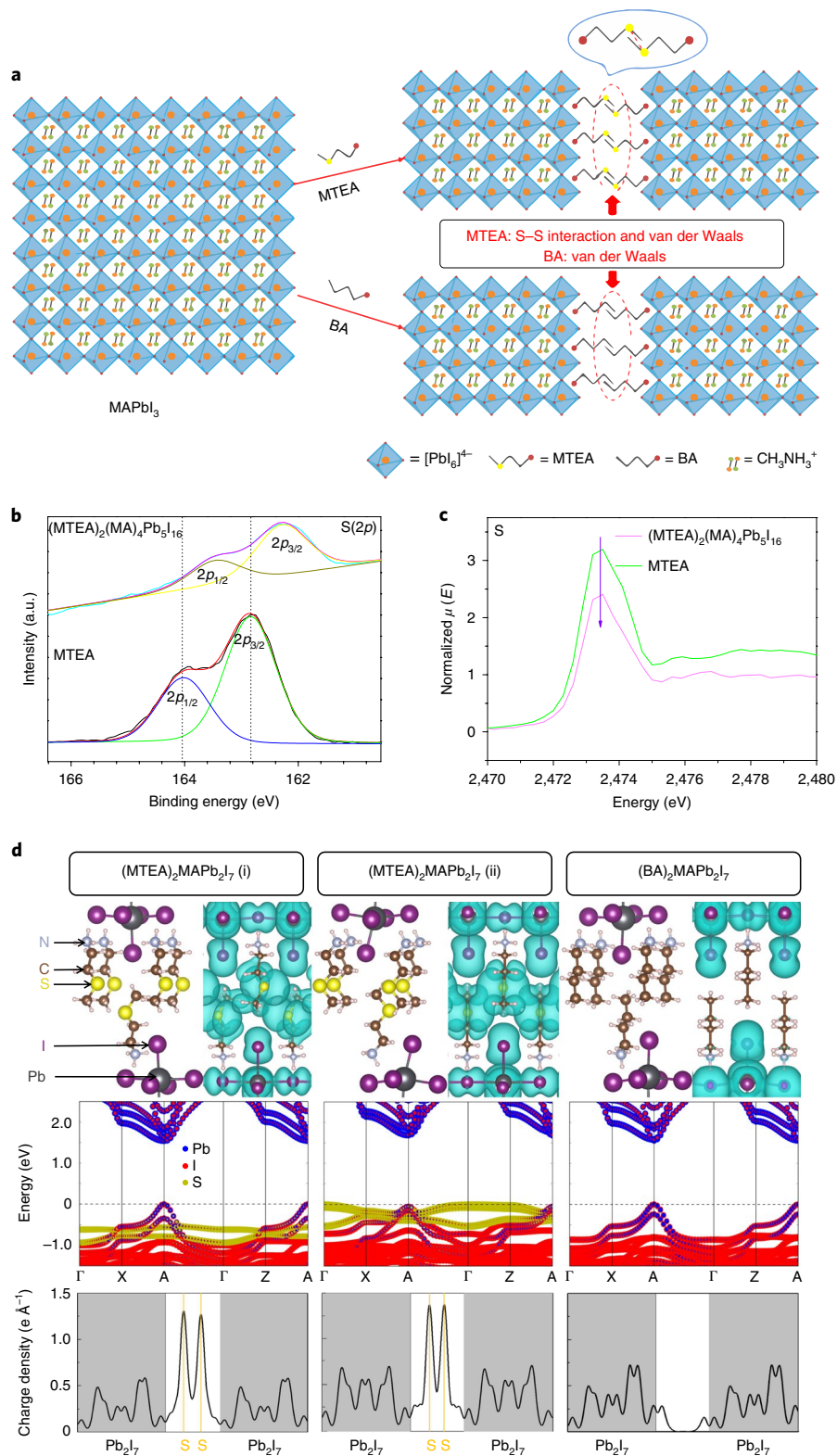


Fig. 1 | Crystal structures and DFT calculations for the 2DRP perovskites. **a**, Schematic crystal structures of the 2DRP perovskites (MTEA)₂(MA)_{*n*-1}Pb_{*n*}I_{3*n*+1} and (BA)₂(MA)_{*n*-1}Pb_{*n*}I_{3*n*+1}. **b**, A comparison of X-ray photoelectron spectroscopy (XPS) spectra of the S(2p) of the MTEACl films and (MTEA)₂(MA)₄Pb₅I₁₆ perovskite films. **c**, A comparison of X-ray absorption near edge structure (XANES) spectra of the S element of MTEACl films and (MTEA)₂(MA)₄Pb₅I₁₆ perovskite films. μ is the X-ray absorption coefficient at and above the absorption edge of a selected element and E is energy. **d**, First-principles DFT calculations for the 2DRP (MTEA)₂(MA)_{*n*-1}Pb_{*n*}I_{3*n*+1} perovskites with $n=2$, (MTEA)₂MAPb₂I₇, compared with the counterpart (BA)₂MAPb₂I₇. For (MTEA)₂MAPb₂I₇, the results of two structures with comparable low energies (see main text) are shown. For each material, the crystal structure and 3D charge density around the valence band edge (upper panels), electronic band structure projected onto the composed atoms (middle panels) and planar-averaged charge density distribution perpendicular to the perovskite layers (bottom panels) are shown. The charge density shown is the partial charge density integral within 1 eV below the valence band maximum.

tures from $n = 1$ to 4, with relatively high roughness (Supplementary Fig. 4) and pinholes, indicating the obvious RP phase layered structure, whereas for $n > 4$ the films tend to be smoother and denser with fewer pinholes. For $n = 5$, the 2DRP perovskite films are compact and flat with no pinholes; they also have an average crystal grain size of 600 nm and super low roughness of 0.863 nm, competitive with those of organic films⁶. This result further confirms that high-quality 2DRP perovskites can be achieved. However, an increased number of pinholes is observed in the $n = 6$ 2DRP film, which may result in current leakage as a result of direct contact of the hole and electron transporting layers in PSCs, thus probably resulting in poor device performance.

To further investigate the effect of MTEA on the crystallization of 2DRP perovskites, X-ray diffraction (XRD) was performed to characterize the perovskite crystallization and phases (Supplementary Fig. 5). This analysis characteristically revealed an additional low-angle reflection for perovskites with small layer numbers ($n = 1$ and 2), which is the unambiguous signature of the layered structure²⁶. Moreover, a transformation from uniform 2D perovskite phases to multiple 2D perovskite phases was observed from $n = 1$ to $n = 2$ (refs. 8–11,21,23). This is evidenced by the appearance of $\langle 111 \rangle$ and $\langle 202 \rangle$ peaks, representative of the out-of-plane growth of thick perovskite segments, that is, 2D perovskite phase with large n due to the incorporation of MA²¹. As the layer number increases ($n > 2$), the growth of the low-diffraction-angle 2D phase is gradually replaced by the growth of the $\langle 111 \rangle$ and $\langle 202 \rangle$ crystal planes, which indicates vertical growth of the 2DRP perovskites with respect to the substrate²⁷. This growth can be attributed to the competition between the MTEA cations that limit growth in the planar layer and the MA cations that attempt to extend the out-of-plane perovskite growth²¹. The oriented growth of perovskite films along the $\langle 111 \rangle$ and $\langle 202 \rangle$ planes also indicates the high degree of crystallinity of the film, which benefits the formation of high-quality films, consistent with SEM and atomic force microscopy (AFM) results. The formation of the RP phase layered structure can be further confirmed by the observation of sharp excitonic absorption peaks for 2DRP perovskites with different layer numbers (Supplementary Fig. 6), in agreement with previous reports²⁸. Mixed few-layer RP phases (for example, $n = 2$ and 3) can be observed in a higher-layer-number structure ($n = 5$), showing that obtaining the pure single RP phase is difficult, even based on a fixed stoichiometric molar ratio of raw materials^{9,20,29,30}.

We also investigated the crystallinity and oriented growth of the perovskite films using grazing incidence wide-angle X-ray scattering (GIWAXS) imaging, as shown in Fig. 2. The 3D films exhibit diffraction rings with stronger intensities along certain extended arc segments (Fig. 2a), which indicates considerable random crystal orientation in the thin films and agrees with previous reports³¹. In contrast, the BA-based perovskite films show discrete Bragg spots along the same rings (Fig. 2b), suggesting ordered alignment of crystals in the thin films. As shown in Fig. 2c, the MTEA-based perovskite films also exhibit much sharper and more discrete Bragg spots (indicating single crystalline-like domains) compared to both the BA and 3D counterparts. This result strongly suggests that the highly oriented growth of the RP phases with inorganic components is perpendicular to the substrate, leading to the formation of continuous charge transport channels and allowing efficient charge transport and extraction in the vertical direction⁸. Moreover, in comparison to the BA perovskite films, in which the pole figures of the azimuth angle show three arcs along the same rings at 90°, 137° and 180° (Supplementary Fig. 7), the MTEA perovskite films show two distinct arcs at azimuth angles of 90° and 180°, further indicating the high crystallization and orientation of the MTEA-based 2DRP perovskites. The corresponding schematic diagrams of 3D and BA- and MTEA-based perovskite films with different orientations are presented in Fig. 2d–f. The results strongly

demonstrate that the S–S interaction in MTEA can stabilize and tighten the framework of the 2DRP perovskite phase to allow vertically oriented growth.

Charge transfer dynamics and charge transport characteristics. To explore whether the S–S interaction can enhance the photoelectronic properties of the $(\text{MTEA})_2(\text{MA})_4\text{Pb}_5\text{I}_{16}$ over $(\text{BA})_2(\text{MA})_4\text{Pb}_5\text{I}_{16}$ ($n = 5$) 2DRP perovskites, the trap state density, charge carrier mobility and charge transfer kinetics were investigated. The exciton lifetime and charge quenching of 2DRP perovskite heterojunctions with poly(3,4-ethylenedioxythiophene) polystyrene sulfonate (PEDOT:PSS) and [6,6]-phenyl-C₆₁-butyric acid methyl ester (PC₆₁BM) were first studied. As shown in Fig. 3a, the pure $(\text{MTEA})_2(\text{MA})_4\text{Pb}_5\text{I}_{16}$ 2DRP perovskite film shows an exciton lifetime of $\tau_e = 122$ ns, which is well quenched by PEDOT:PSS and PC₆₁BM to lifetimes of $\tau_e = 3.18$ ns and $\tau_e = 2.34$ ns. In comparison, the $(\text{BA})_2(\text{MA})_4\text{Pb}_5\text{I}_{16}$ perovskite film shows exciton lifetimes of 108 ns for the bare film and 6.29 ns and 2.48 ns for the heterojunctions with PEDOT:PSS and PC₆₁BM, respectively (Fig. 3b). The longer lifetime of $(\text{MTEA})_2(\text{MA})_4\text{Pb}_5\text{I}_{16}$ compared to that of $(\text{BA})_2(\text{MA})_4\text{Pb}_5\text{I}_{16}$ demonstrates the high crystal quality of the $(\text{MTEA})_2(\text{MA})_4\text{Pb}_5\text{I}_{16}$ 2DRP perovskites. The faster photoluminescence (PL) decay in the PEDOT:PSS and PC₆₁BM heterojunctions with 2DRP perovskites further indicates the effective charge extraction of $(\text{MTEA})_2(\text{MA})_4\text{Pb}_5\text{I}_{16}$ compared to $(\text{BA})_2(\text{MA})_4\text{Pb}_5\text{I}_{16}$, which is related to the highly oriented RP phases in the $(\text{MTEA})_2(\text{MA})_4\text{Pb}_5\text{I}_{16}$ 2DRP perovskites. The charge carrier transfer time (τ_{CT}) and efficiency were estimated to be 3.27 ns and 97% (ref. 32), respectively, for the $(\text{MTEA})_2(\text{MA})_4\text{Pb}_5\text{I}_{16}$ perovskites, while the $(\text{BA})_2(\text{MA})_4\text{Pb}_5\text{I}_{16}$ perovskites gave values of 6.67 ns and as low as 94% (Supplementary Table 2). It should be noted that the PC₆₁BM exhibits better exciton quenching than PEDOT:PSS in 2DRP perovskites, demonstrating the great possibility for optimization of the hole–electron contact.

Moreover, a lower trap density and a higher charge mobility are also observed in $(\text{MTEA})_2(\text{MA})_4\text{Pb}_5\text{I}_{16}$ compared to $(\text{BA})_2(\text{MA})_4\text{Pb}_5\text{I}_{16}$ perovskites based on space charge limited current (SCLC) measurements on electron-only and hole-only devices, as shown in Fig. 3c,d. We collected the dark current–voltage characteristics for both electron-only devices (indium tin oxide (ITO)/SnO₂ (10 nm)/2DRP perovskite (350 nm)/PC₆₁BM (80 nm)/LiF (1 nm)/Al (100 nm)) and hole-only devices (ITO/PEDOT:PSS (40 nm)/2DRP perovskite (350 nm)/poly(9,9-dioctyl-fluorene-co-N-(4-butylphenyl)diphenylamine) (TFB) (80 nm)/MoO₃ (8 nm)/Al (100 nm)). The trap state density is determined by the trap-filled limit (TFL) voltage using the equation³³

$$N_t = \frac{2\epsilon_0\epsilon_r V_{\text{TFL}}}{qL^2}$$

where ϵ_0 is the vacuum permittivity, ϵ_r is the relative dielectric constant, V_{TFL} is the onset voltage of the TFL region, q is the elemental charge and L is the thickness of the film. We found that the electron and hole trap densities significantly decrease from $6.67 \times 10^{15} \text{ cm}^{-3}$ to $2.22 \times 10^{15} \text{ cm}^{-3}$ and from $9.92 \times 10^{15} \text{ cm}^{-3}$ to $5.18 \times 10^{15} \text{ cm}^{-3}$ from the $(\text{BA})_2(\text{MA})_4\text{Pb}_5\text{I}_{16}$ to $(\text{MTEA})_2(\text{MA})_4\text{Pb}_5\text{I}_{16}$ perovskites (Supplementary Table 3), respectively. Moreover, to investigate which recombination dominates³⁴, for example, trap-assisted Shockley–Read–Hall recombination or bimolecular recombination, the dependences of the short-circuit current (J_{sc}) and open-circuit voltage (V_{oc}) on light intensity were obtained (Supplementary Fig. 8). We found a good linear relationship between J_{sc} and light intensity, with slopes of 0.92 and 0.94 for the $(\text{BA})_2(\text{MA})_4\text{Pb}_5\text{I}_{16}$ and $(\text{MTEA})_2(\text{MA})_4\text{Pb}_5\text{I}_{16}$ devices, respectively; these values are close to 1, indicating that the bimolecular recombination in the devices is almost negligible. In contrast, the slopes in the V_{oc} versus light

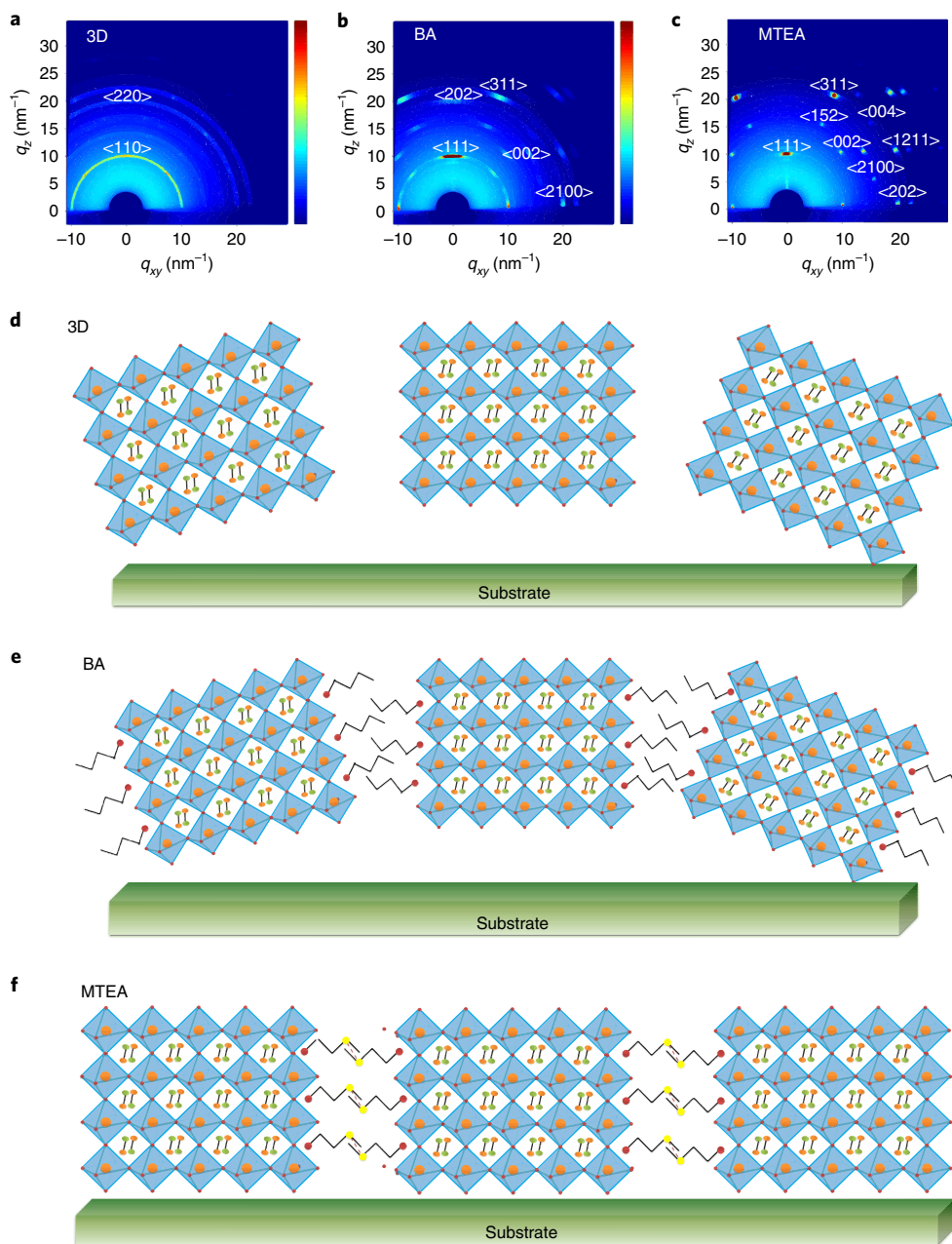


Fig. 2 | GIWAXS patterns for the 3D and 2DRP perovskite films. a–c, GIWAXS patterns of 3D (a), $(\text{BA})_2(\text{MA})_4\text{Pb}_5\text{I}_{16}$ (b) and $(\text{MTEA})_2(\text{MA})_4\text{Pb}_5\text{I}_{16}$ (c) perovskite films. The colour bars represent the diffraction intensity. **d–f,** Schematics from random orientation to vertical orientation of 3D (d), $(\text{BA})_2(\text{MA})_4\text{Pb}_5\text{I}_{16}$ (e) and $(\text{MTEA})_2(\text{MA})_4\text{Pb}_5\text{I}_{16}$ (f) perovskite films.

intensity curves reach 0.12 for the $(\text{BA})_2(\text{MA})_4\text{Pb}_5\text{I}_{16}$ device and only ~ 0.07 for the $(\text{MTEA})_2(\text{MA})_4\text{Pb}_5\text{I}_{16}$ device, indicating that MTEA can significantly reduce trap-assisted recombination in the device, in agreement with the observation from SCLC measurements (Fig. 3c,d) that MTEA can help reduce the trap state density of the perovskite films.

We further calculated the charge carrier mobility of 2DRP perovskite films, which was well fitted by the Mott–Gurney Law³⁵:

$$J = \frac{9\varepsilon_0\varepsilon_r\mu V^2}{8L^3}$$

where μ is the charge mobility and V is the applied voltage. Compared to $(\text{BA})_2(\text{MA})_4\text{Pb}_5\text{I}_{16}$ perovskites, the $(\text{MTEA})_2(\text{MA})_4\text{Pb}_5\text{I}_{16}$ perovskites give higher electron and hole mobilities

of $1.3 \times 10^{-2} \text{ cm}^2 \text{ V}^{-1} \text{ s}^{-1}$, compared to $0.56 \times 10^{-2} \text{ cm}^2 \text{ V}^{-1} \text{ s}^{-1}$, and $1.7 \times 10^{-2} \text{ cm}^2 \text{ V}^{-1} \text{ s}^{-1}$, compared to $1.5 \times 10^{-2} \text{ cm}^2 \text{ V}^{-1} \text{ s}^{-1}$ (Supplementary Table 3). This result can be attributed to the excellent film quality, as demonstrated by SEM and AFM and the highly oriented growth of the $(\text{MTEA})_2(\text{MA})_4\text{Pb}_5\text{I}_{16}$ 2DRP perovskite films. Two charge transport channels need to be taken into account³⁶: transport along the inorganic component and transport across the bulky alkylammonium between PbI_6 octahedra. In addition to the vertical orientation of the $(\text{MTEA})_2(\text{MA})_4\text{Pb}_5\text{I}_{16}$ 2DRP perovskite films, which facilitates charge transport, the S–S interaction in MTEA also enhances charge transport across MTEA molecules (Fig. 3e). However, the charge transport across the BA molecules in $(\text{BA})_2(\text{MA})_4\text{Pb}_5\text{I}_{16}$ 2DRP perovskite films is highly limited by the less oriented growth due to the weak van der Waals interaction between BA molecules (Fig. 3f). The impedance spectra of the

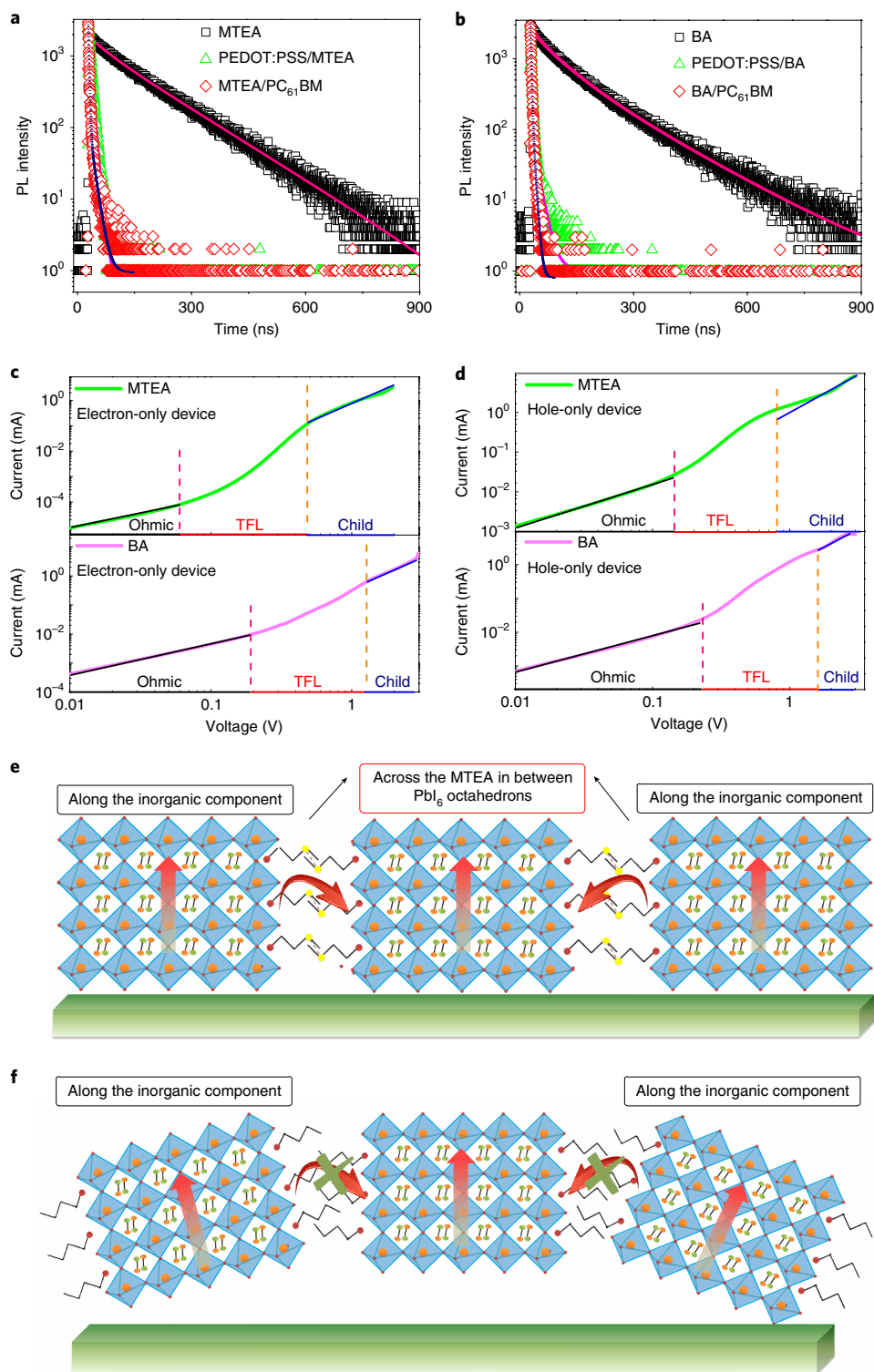


Fig. 3 | Charge transfer dynamics and charge transport characteristics. **a,b**, Time-resolved PL spectra of (MTEA)₂(MA)₄Pb₅I₁₆ (**a**) and (BA)₂(MA)₄Pb₅I₁₆ (**b**) 2DRP perovskite films and their heterojunction with PEDOT:PSS and PC₆₁BM on quartz plates. **c,d**, Current-voltage curves of electron-only devices for (MTEA)₂(MA)₄Pb₅I₁₆ and (BA)₂(MA)₄Pb₅I₁₆ perovskite (**c**) and hole-only devices for (MTEA)₂(MA)₄Pb₅I₁₆ and (BA)₂(MA)₄Pb₅I₁₆ perovskites (**d**). The electron-only device structure is ITO/SnO₂ (20 nm)/2DRP perovskite (350 nm)/PC₆₁BM (80 nm)/LiF (1 nm)/Al (100 nm). The hole-only device structure is ITO/PEDOT:PSS (40 nm)/2DRP perovskite (350 nm)/TFB (80 nm)/MoO₃ (8 nm)/Al (100 nm). TFL, trap-filled limit; Child, trap-free Child's region. **e,f**, Schematics of charge transport of MTEA (**e**) and BA (**f**) based 2D perovskite films.

two types of 2DRP film also confirm the improved charge transport in (MTEA)₂(MA)₄Pb₅I₁₆ perovskite films compared to that in (BA)₂(MA)₄Pb₅I₁₆ perovskite films (Supplementary Fig. 9).

Performance of 2DRP PSCs. The flat, dense and highly oriented crystalline 2DRP perovskite thin films of (MTEA)₂(MA)₄Pb₅I₁₆, with their excellent optical and electrical properties, are particularly

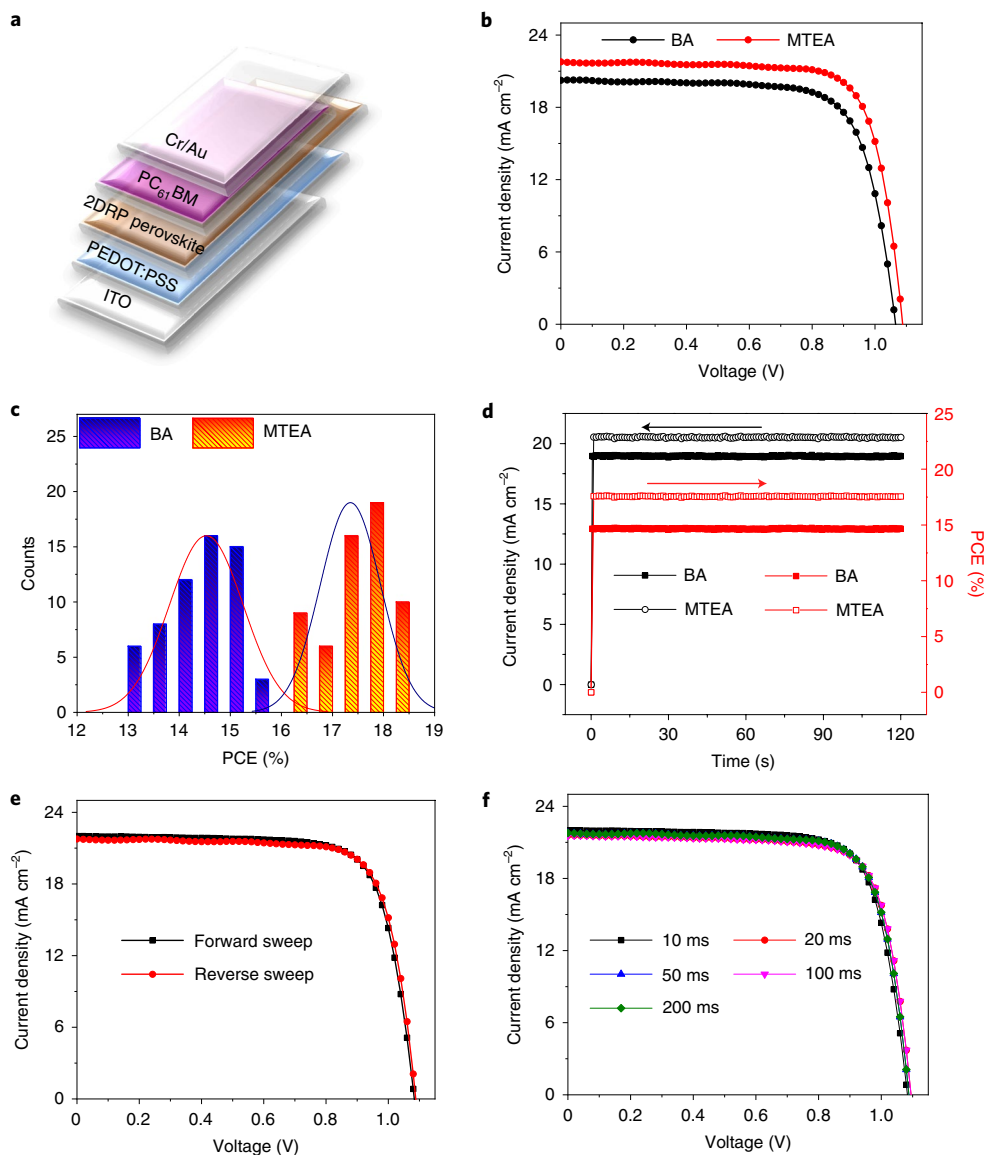


Fig. 4 | 2DRP PSCs architecture and characterization. **a**, Schematic of 2DRP PSCs with a structure of ITO/PEDOT:PSS (40 nm)/2DRP perovskite (350 nm)/PC₆₁BM (80 nm)/Cr (3 nm)/Au (100 nm). **b**, Current density–voltage (*J*–*V*) curves under an AM1.5G solar simulator for devices based on (MTEA)₂(MA)₄Pb₅I₁₆ and (BA)₂(MA)₄Pb₅I₁₆ 2DRP perovskites. **c**, Reproducibility on 60 devices of (MTEA)₂(MA)₄Pb₅I₁₆ and (BA)₂(MA)₄Pb₅I₁₆ 2DRP perovskites. **d**, Stabilized photocurrent and steady efficiency at the maximum power output point (0.90 V and 0.88 V) of the (MTEA)₂(MA)₄Pb₅I₁₆ and (BA)₂(MA)₄Pb₅I₁₆ 2DRP PSCs. **e, f**, *J*–*V* curves of (MTEA)₂(MA)₄Pb₅I₁₆ 2DRP PSCs with different scanning directions (forward, black line; reverse, red line) (**e**) and with different delay times (**f**).

suitable for preparing photovoltaic devices. We therefore fabricated planar heterojunction devices with the structure ITO/PEDOT:PSS (40 nm)/2DRP perovskite (350 nm)/PC₆₁BM (80 nm)/Cr (3 nm)/Au (100 nm), as shown in Fig. 4a. The current–voltage (*J*–*V*) curves of the devices were recorded using simulated AM1.5G solar illumination. The best-performing PSCs based on (MTEA)₂(MA)₄Pb₅I₁₆ exhibited a high PCE of 18.06% with *V*_{oc} of 1.088 V, *J*_{sc} of 21.77 mA cm⁻² and a fill factor (FF) of 76.27%; these values are remarkably higher than those of the (BA)₂(MA)₄Pb₅I₁₆-based device, with its relatively low PCE of 15.94%, *V*_{oc} of 1.065 V, *J*_{sc} of 20.25 mA cm⁻² and FF of 73.85%. The high PCE of 18.06% is one of the best reported efficiencies, to our knowledge (Supplementary Table 4). To confirm the reliability of our efficiency measurements, one of our non-encapsulated devices was sent to the National Institute of Metrology in China for certification and a PCE of 17.80% was confirmed (*J*_{sc} of 21.38 mA cm⁻², *V*_{oc} of 1.084 V and FF of 76.8%; Supplementary

Fig. 10). The performance improvement is mainly attributed to the enhanced *J*_{sc} in the (MTEA)₂(MA)₄Pb₅I₁₆-based devices (Fig. 4b), which is a consequence to the highly vertically oriented and high-quality 2DRP perovskite films (Supplementary Fig. 11) with low trap density and high charge mobility induced by the S–S interaction. Note that the dark features in the films are shallow holes, not pinholes, as confirmed by cross-sectional SEM of the complete devices (Supplementary Fig. 12). The current density was calculated based on the incident photon-to-current efficiency and matches the *J*_{sc} well (Supplementary Fig. 13). Moreover, we fabricated 60 devices using 2DRP (MTEA)₂(MA)₄Pb₅I₁₆ and (BA)₂(MA)₄Pb₅I₁₆ perovskites, which showed average PCEs of 17.35% and 14.51%, respectively (Fig. 4c, Supplementary Figs. 14 and 15 and Supplementary Table 1), demonstrating the reproducibility of our 2DRP PSCs. We also fabricated devices with an area of 1 cm⁻², and the best PCE achieved was 16.77%, with an average PCE of 15.81% (Supplementary Fig. 16).

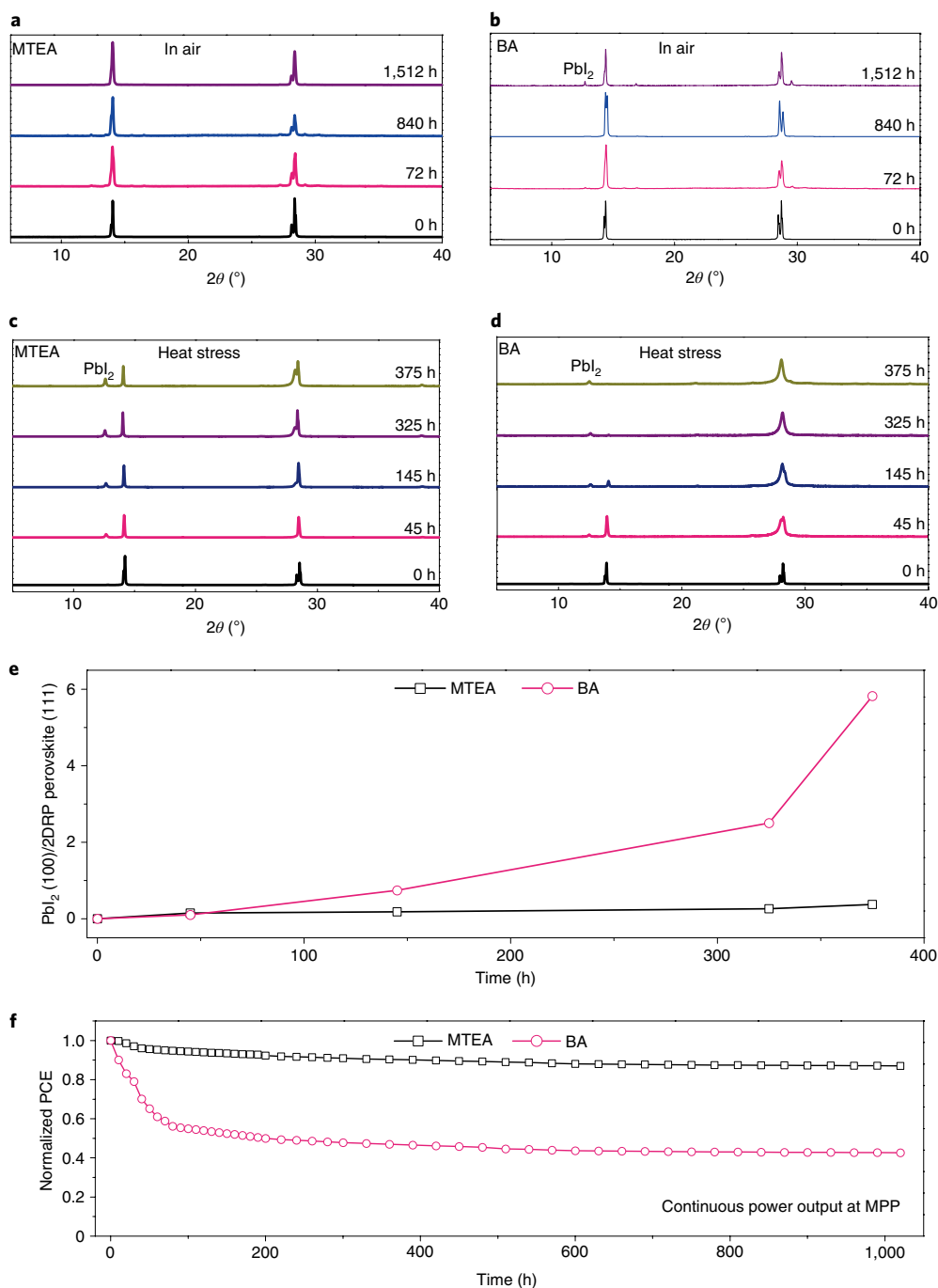


Fig. 5 | Stability of $(\text{MTEA})_2(\text{MA})_4\text{Pb}_5\text{I}_{16}$ and $(\text{BA})_2(\text{MA})_4\text{Pb}_5\text{I}_{16}$ 2DRP thin films and PSCs. a,b, Air stability of $(\text{MTEA})_2(\text{MA})_4\text{Pb}_5\text{I}_{16}$ (a) and $(\text{BA})_2(\text{MA})_4\text{Pb}_5\text{I}_{16}$ (b) thin films, fabricated and tested in a room-temperature and 80% ($\pm 7\%$) relative humidity ambient atmosphere, completely without encapsulation. **c,d**, Heat stability of $(\text{MTEA})_2(\text{MA})_4\text{Pb}_5\text{I}_{16}$ (c) and $(\text{BA})_2(\text{MA})_4\text{Pb}_5\text{I}_{16}$ (d) perovskite thin films under continuous heat at 85 °C. **e**, Ratio of the PbI_2 ($2\theta = 12.7^\circ$ referred to $\langle 100 \rangle$) and perovskite ($2\theta = 14.2^\circ$ referred to $\langle 111 \rangle$) main peaks in **c** and **d** for the two perovskites over 375 h. **f**, Operational stability of non-encapsulated 2DRP $(\text{MTEA})_2(\text{MA})_4\text{Pb}_5\text{I}_{16}$ and $(\text{BA})_2(\text{MA})_4\text{Pb}_5\text{I}_{16}$ PSCs in a N_2 -filled glovebox. The devices were examined at the MPP (0.90 V and 0.88 V for $(\text{MTEA})_2(\text{MA})_4\text{Pb}_5\text{I}_{16}$ and $(\text{BA})_2(\text{MA})_4\text{Pb}_5\text{I}_{16}$ devices, respectively) under continuous 1 sun, AM1.5G illumination.

This result shows a small PCE decrease and high device yield, indicating that our approach is impressive in terms of scalability for commercialization and large-scale devices. The stabilized photocurrent and steady efficiency at the MPP (0.90 V) were measured (Fig. 4d). The photocurrent density immediately reaches 20.53 mA cm^{-2} on light irradiation, resulting in a stabilized PCE of 17.17%, and is maintained constant under continuous illumination, demonstrating the reliability of our devices. Moreover, negligible

photocurrent hysteresis can be observed in our devices, as indicated by the similar J - V curves under different scan rates and scan directions (Fig. 4e,f), which can be attributed to the low trap density and passivation of PC_{61}BM , in good agreement with previous reports³⁴.

Long-term stability of 2DRP perovskites. We performed long-term stability tests of $(\text{MTEA})_2(\text{MA})_4\text{Pb}_5\text{I}_{16}$ and $(\text{BA})_2(\text{MA})_4\text{Pb}_5\text{I}_{16}$ 2DRP perovskite films under humidity and heat stress. The

(MTEA)₂(MA)₄Pb₅I₁₆ perovskites show no change in XRD patterns when exposed to ambient air for even 1,512 h under a humidity of 80% (Fig. 5a), while the (BA)₂(MA)₄Pb₅I₁₆ 2DRP perovskite films have a significant PbI₂ peak (Fig. 5b), indicating that degradation has started. Moreover, a small PbI₂ peak is observed in the (MTEA)₂(MA)₄Pb₅I₁₆ 2DRP perovskite films maintained under continuous heat at 85 °C for 45 h, with no significant change after 375 h (Fig. 5c,e). However, serious degradation of (BA)₂(MA)₄Pb₅I₁₆ 2DRP perovskite films under heat is demonstrated by the remarkable enhancement of the PbI₂ peak accompanied by the disappearance of the <111> peak (Fig. 5d,e). Obviously, the S–S interaction can markedly stabilize the framework of 2DRP perovskites and improve the humidity and heat stability.

To further demonstrate the merit of the S–S interaction in stabilizing the framework of 2DRP perovskites, we conducted a stability test in or close to the harsh industry standard conditions^{37–39}. For the moisture tolerance test, the two types of 2DRP perovskite film were placed in a constant temperature and humidity box at 85% humidity and 85 °C in air. As shown in Supplementary Fig. 17, the (BA)₂(MA)₄Pb₅I₁₆ perovskite films have completely degraded to PbI₂ after 24 h, while the (MTEA)₂(MA)₄Pb₅I₁₆ perovskite films still retains strong (111) and (202) peaks, with the appearance of small PbI₂ peaks. For the thermal stability test, the two types of 2DRP perovskite film were maintained under continuous heat at 150 °C in a N₂-filled glovebox. As shown in Supplementary Fig. 18, the (BA)₂(MA)₄Pb₅I₁₆ perovskite films have almost degraded to PbI₂ after 48 h, while no serious degradation of the (MTEA)₂(MA)₄Pb₅I₁₆ perovskite films is observed. These results indicate the potential real application of our 2DRP perovskite films in such harsh conditions.

Most importantly, we performed device stability measurements under operational conditions at the MPP for MTEA- and BA-based devices (0.90 V and 0.88 V, respectively) under continuous 1 sun, AM1.5G illumination in a N₂-filled glovebox. As shown in Fig. 5f, the BA-based device degrades rapidly at the MPP, with a 40% decrease from its initial efficiency within 70 h, and the efficiency finally remains at ~40% of the initial efficiency after 1,000 h. In contrast, the MTEA-based device retains 87.1% of its initial efficiency after continuous power output at the MPP for 1,000 h with a constant load of 0.90 V. This result is one of the best stabilities achieved in a device at the MPP for 1,000 h, to our knowledge^{8,40,41}. We attribute the improved stability of the 2DRP (MTEA)₂(MA)₄Pb₅I₁₆ over (BA)₂(MA)₄Pb₅I₁₆ PSCs to the S–S interaction markedly stabilizing the framework of 2DRP perovskites, which induces a highly oriented crystal (Fig. 2) with few unintentional defects (Fig. 3c,d) and improved heat stability (Fig. 5c,d). It should be noted that the device temperature is kept at ~25 °C under continuous 1 sun, AM1.5G illumination.

Conclusions

In this work, we have shown that interactions among the organic tails of the ammonium molecules play an important role in constructing efficient and stable 2DRP hybrid perovskites. Efficient intercalated 2DRP hybrid perovskites stabilized by the S–S interaction are reported. The 2DRP perovskite films with strong out-of-plane preferential growth induced by the S–S interaction typically enable efficient charge transport, effective charge separation and low trap density. Moreover, the strengthened interlayer molecular interaction yields 2DRP perovskites stable to temperatures well above 85 °C, rendering the 2DRP perovskites a particularly interesting family of materials. The discovered interlayer interactions of 2DRP perovskites provide a particularly flexible framework and an alternative opportunity to tailor this scientifically and technologically interesting class of hybrid perovskites for potential applications.

Online content

Any methods, additional references, Nature Research reporting summaries, source data, extended data, supplementary information,

acknowledgements, peer review information; details of author contributions and competing interests; and statements of data and code availability are available at <https://doi.org/10.1038/s41566-019-0572-6>.

Received: 5 December 2018; Accepted: 26 November 2019;

Published online: 13 January 2020

References

- Smith, I. C., Hoke, E. T., Solis-Ibarra, D., McGehee, M. D. & Karunadasa, H. I. A layered hybrid perovskite solar-cell absorber with enhanced moisture stability. *Angew. Chem. Int. Ed.* **53**, 11232–11235 (2014).
- Zhou, Y. et al. Benzylamine-treated wide-bandgap perovskite with high thermal-photo stability and photovoltaic performance. *Adv. Energy Mater.* **7**, 1701048 (2017).
- Peng, W. et al. Ultralow self-doping in two-dimensional hybrid perovskite single crystals. *Nano Lett.* **17**, 4759–4767 (2017).
- Lin, Y. et al. Suppressed ion migration in low-dimensional perovskites. *ACS Energy Lett.* **2**, 1571–1572 (2017).
- Cheng, Z. & Lin, J. Layered organic–inorganic hybrid perovskites: structure, optical properties, film preparation, patterning and templating engineering. *CrystEngComm* **12**, 2646–2662 (2010).
- Stoumpos, C. C. et al. High members of the 2D Ruddlesden–Popper halide perovskites: synthesis, optical properties and solar cells of (CH₃(CH₂)₃NH₂)₂(CH₃NH₂)₂Pb₅I₁₆. *Chem* **2**, 427–440 (2017).
- Stoumpos, C. C. et al. Ruddlesden–Popper hybrid lead iodide perovskite 2D homologous semiconductors. *Chem. Mater.* **28**, 2852–2867 (2016).
- Tsai, H. et al. High-efficiency two-dimensional Ruddlesden–Popper perovskite solar cells. *Nature* **536**, 312–316 (2016).
- Proppe, A. H. et al. Synthetic control over quantum well width distribution and carrier migration in low-dimensional perovskite photovoltaics. *J. Am. Chem. Soc.* **140**, 2890–2896 (2018).
- Lai, H. et al. Two-dimensional Ruddlesden–Popper perovskite with nanorod-like morphology for solar cells with efficiency exceeding 15%. *J. Am. Chem. Soc.* **140**, 11639–11646 (2018).
- Yang, R. et al. Oriented quasi-2D perovskites for high performance optoelectronic devices. *Adv. Mater.* **30**, 1804771 (2018).
- Zhang, J. et al. Uniform permutation of quasi-2D perovskites by vacuum poling for efficient, high-fill-factor solar cells. *Joule* **3**, 1–11 (2019).
- Eiichi, H. & Naoto, N. Quantum wells with enhanced exciton effects and optical non-linearity. *Mater. Sci. Eng.* **1**, 255–288 (1988).
- Hong, X., Ishihara, T. & Nurmikko, A. V. Photoconductivity and electroluminescence in lead iodide based natural quantum well structures. *Solid State Commun.* **84**, 657–661 (1992).
- Masaki, S. & Satoru, S. Interband optical transitions in extremely anisotropic semiconductors. *J. Phys. Soc. Jpn* **21**, 1936–1946 (1966).
- Kamminga, M. E. et al. Confinement effects in low-dimensional lead iodide perovskite hybrids. *Chem. Mater.* **28**, 4554–4562 (2016).
- Smith, I. C., Smith, M. D., Jaffe, A., Lin, Y. & Karunadasa, H. I. Between the sheets: post synthetic transformations in hybrid perovskites. *Chem. Mater.* **29**, 1868–1884 (2017).
- Mitzi, D. B., Dimitrakopoulos, C. D. & Kosbar, L. L. Structurally tailored organic–inorganic perovskites: optical properties and solution-processed channel materials for thin-film transistors. *Chem. Mater.* **13**, 3728–3740 (2001).
- Even, J., Pedesseau, L. & Katan, C. Understanding quantum confinement of charge carriers in layered 2D hybrid perovskites. *ChemPhysChem* **15**, 3733–3741 (2014).
- Ishihara, T. Optical properties of PbI₂-based perovskite structures. *J. Lumin.* **60–61**, 269–274 (1994).
- Quan, L. N. et al. Ligand-stabilized reduced-dimensionality perovskites. *J. Am. Chem. Soc.* **138**, 2649–2655 (2016).
- Cao, D. H., Stoumpos, C. C., Farha, O. K., Hupp, J. T. & Kanatzidis, M. G. 2D homologous perovskites as light-absorbing materials for solar cell applications. *J. Am. Chem. Soc.* **137**, 7843–7850 (2015).
- Yao, K., Wang, X., Xu, Y., Li, F. & Zhou, L. Multilayered perovskite materials based on polymeric-ammonium cations for stable large-area solar cell. *Chem. Mater.* **28**, 3131–3138 (2016).
- Hitchcock, A. P., Bodeu, S. & Tronc, M. Sulfur and chlorine K-shell spectra of gases. *Physica B* **158**, 257–258 (1989).
- Steudel, R. Properties of sulfur–sulfur bonds. *Angew. Chem. Int. Ed.* **14**, 655–720 (1975).
- Koh, T. M. et al. High stability bilayered perovskites through crystallization driven self-assembly. *ACS Appl. Mater. Interfaces* **9**, 28743–28749 (2017).
- Soe, C. M. M. et al. Understanding film formation morphology and orientation in high member 2D Ruddlesden–Popper perovskites for high-efficiency solar cells. *Adv. Energy Mater.* **8**, 1700979 (2017).

28. Shang, Q. et al. Unveiling structurally engineered carrier dynamics in hybrid quasi-two-dimensional perovskite thin films toward controllable emission. *J. Phys. Chem. Lett.* **8**, 4431–4438 (2017).
29. Liao, Y. et al. Highly oriented low-dimensional tin halide perovskites with enhanced stability and photovoltaic performance. *J. Am. Chem. Soc.* **139**, 6693–6699 (2017).
30. Zhang, X. et al. Phase transition control for high performance Ruddlesden–Popper perovskite solar cells. *Adv. Mater.* **30**, 1707166 (2018).
31. Zheng, H. et al. The effect of hydrophobicity of ammonium salts on stability of quasi-2D perovskite materials in moist condition. *Adv. Energy Mater.* **8**, 1800051 (2018).
32. Xing, G. et al. Long-range balanced electron-and hole-transport lengths in organic–inorganic $\text{CH}_3\text{NH}_3\text{PbI}_3$. *Science* **342**, 344–347 (2013).
33. Shi, D. et al. Low trap-state density and long carrier diffusion in organolead trihalide perovskite single crystals. *Science* **347**, 519–522 (2015).
34. Liu, Y. et al. A dopant-free organic hole transport material for efficient planar heterojunction perovskite solar cells. *J. Mater. Chem. A* **3**, 11940–11947 (2015).
35. Dong, Q. et al. Electron-hole diffusion lengths $>175\mu\text{m}$ in solution-grown $\text{CH}_3\text{NH}_3\text{PbI}_3$ single crystals. *Science* **347**, 967–970 (2015).
36. Ma, C., Shen, D., Ng, T., Lo, M. & Lee, C. 2D perovskites with short interlayer distance for high-performance solar cell application. *Adv. Mater.* **30**, 1800710 (2018).
37. Domanski, K., Alharbi, E. A., Hagfeldt, A., Grätzel, M. & Tress, W. Systematic investigation of the impact of operation conditions on the degradation behaviour of perovskite solar cells. *Nat. Energy* **3**, 61–67 (2018).
38. Ono, L. K., Qi, Y. & Liu, S. Progress toward stable lead halide perovskite solar cells. *Joule* **2**, 1961–1990 (2018).
39. Saliba, M. Perovskite solar cells must come of age. *Science* **359**, 388–389 (2018).
40. Grancini, G. et al. One-year stable perovskite solar cells by 2D/3D interface engineering. *Nat. Commun.* **8**, 15684 (2017).
41. Li, X. et al. In-situ cross-linking strategy for efficient and operationally stable methylammonium lead iodide solar cells. *Nat. Commun.* **9**, 3806 (2018).

Publisher's note Springer Nature remains neutral with regard to jurisdictional claims in published maps and institutional affiliations.

© The Author(s), under exclusive licence to Springer Nature Limited 2020

Methods

Materials. PEDOT:PSS and PC₆₁BM were purchased from Clevious and Nano-C, respectively. Lead iodide (PbI₂, 99.99%) was purchased from TCI. Butylamine hydrochloride, 2-(methylthio)ethylamine hydrochloride, methylamine hydrochloride, hydriodic acid (HI, 57 wt% in H₂O), methylamine solution (MA, 33% in H₂O) and ethylic acid (HAc, 99%) were purchased from Sigma-Aldrich. All materials were used as received without further purification.

First-principles calculations. The first-principles calculations were performed using the plane-wave pseudopotential method within the framework of DFT as implemented in the Vienna Ab initio Simulation Package^{42,43}. The electron–ion interaction was described using frozen-core projected augmented-wave pseudopotentials⁴⁴. The electron configurations of 1s for H, 2s²2p² for C, 2s²2p³ for N, 3s²3p⁴ for S, 5s²5p⁵ for I and 6s²6p² for Pb were considered as the valence electrons. The generalized gradient approximation formulated by Perdew, Burke and Ernzerhof was used as the exchange correlation functional⁴⁵. We used a kinetic energy cutoff of 400 eV for wavefunction expansion and a 4 × 4 × 1 Monkhorst–Pack *k*-point mesh for electronic Brillouin zone integration of 2DRP hybrid halide perovskites. The structures (including lattice parameters and internal atomic positions) were fully optimized via total energy minimization, with the total energy converged to less than 0.0001 eV. To properly take into account the long-range van der Waals interaction, which is non-negligible for hybrid perovskites involving organic molecules, the van der Waals optB86b functional was adopted⁴⁶.

Device fabrication. The ITO substrates were cleaned using a cleaning agent in deionized water, ultrapure water and an ethanol solution using an ultrasonic instrument, and then dried at 120 °C overnight. The precursor solutions were prepared by mixing a 1:1:1 stoichiometric ratio of PbI₂, MAI and MTEACl (or BACl) in methylamine acetate. The mixed solution was stirred at 60 °C for 2 h. The ITO was first UV-ozone treated for 15 min. PEDOT:PSS (Heraeus) was spin-coated on the ITO at 5,000 r.p.m. for 50 s and annealed at 120 °C for 30 min. (MTEA)₂(MA)₄Pb₃I₁₆ and (BA)₂(MA)₄Pb₃I₁₆ films were fabricated by spin-coating at 4,000 r.p.m. for 20 s on a hot substrate at 100 °C throughout the entire spin-coating process and then annealed at 60 °C to 100 °C for 4 min. The entire preparation process was performed under ambient conditions. The electron transport layer PC₆₁BM in chlorobenzene solution (18 mg ml⁻¹) was deposited onto the perovskite layer by spin-coating at 1,000 r.p.m. for 60 s. Finally, the device was transferred to an evaporator for thermal evaporation of Cr (3 nm) and Au (100 nm) at a pressure of 1 × 10⁻⁴ Pa.

Device characterization. The photovoltaic output of all devices was measured using an AM1.5G (100 mW cm⁻²) solar simulator (Enlitech SS-F5-3A) calibrated using a standard Si photodiode (calibrated and certified by Enlitech). The difference between the solar simulator Enlitech SS-F5-3A spectrum and the standard AM1.5G solar spectrum was calculated by Enlitech. The light current density–voltage (*J*–*V*) curve was obtained using a Keithley 2400 source meter unit in a N₂-filled glovebox at room temperature by scanning the voltage from –0.2 to 1.2 V (forward scan) and then from 1.2 to –0.2 V (reverse scan) with a step of 0.02 V and 5 ms dwell time. No protocol for preconditioning the device before its characterization was followed. Black masks with apertures of 2.5 × 2 mm² were used to define the illuminated active areas of the cells. The mask/aperture area was fixed and could not be changed.

Stability characterization. For the moisture tolerance test, the two types of 2DRP perovskite film were tested at room temperature and 80% (±7%) relative humidity or in a constant temperature and humidity box maintained at 85% humidity and 85 °C in ambient air without any encapsulation. For the thermal stability test, the two types of 2DRP perovskite film were placed on a hotplate at 85 °C or 150 °C in a N₂-filled glovebox. For the light soaking stability tests, the light intensity and device temperature were fixed at 1 sun, AM1.5G illumination and 25 °C, respectively. The stability of the device over time was determined at the maximum power point under simulated AM1.5G light (Enlitech SS-F5-3A) in a N₂-filled glovebox for 1,000 h.

Perovskite film characterization. The UV–vis absorbance spectra of all samples were measured using an Agilent Cary 5000 UV–vis spectrophotometer with an integrating sphere and a Hitachi F-4600 fluorescent spectrophotometer. The time-resolved PL spectra of the perovskite films were obtained using a transient

fluorescence spectrometer (TCSPC) from Edinburgh Instruments (FLS920). XPS measurements were performed using a PHI 5000 VersaProbe III with a micro-focused scanning Al K α X-ray source. Dual beam charge neutralization was applied and the binding energy was corrected by setting the binding energy of the hydrocarbon C 1s feature to 284.8 eV. GIWAXS data were obtained at beamline BL14B1 of the Shanghai Synchrotron Radiation Facility (SSRF). The S K-edge (2,472 eV) XANES spectroscopy measurements of the samples were performed at the beamline (4B7A) of Beijing Synchrotron Radiation Facility (BSRF), Institute of High Energy Physics (IHEP), Chinese Academy of Sciences (CAS). AFM images were taken using a Park XE7 atomic force microscope in non-contact mode. The morphologies of the perovskite films were obtained using SEM (Hitachi S-3400N). XRD patterns were measured using a Japan's Smart Lab diffractometer.

Reporting Summary. Further information on research design is available in the Nature Research Reporting Summary linked to this article.

Data availability

The data that support the plots within this paper and other findings of this study are available from the corresponding authors upon reasonable request

References

- Kresse, G. & Furthmüller, J. Efficiency of ab-initio total energy calculations for metals and semiconductors using a plane-wave basis set. *Comput. Mater. Sci.* **6**, 15–50 (1996).
- Kresse, G. & Furthmüller, J. Efficient iterative schemes for ab initio total-energy calculations using a plane-wave basis set. *Phys. Rev. B* **54**, 11169–11186 (1996).
- Blöchl, P. E. Projector augmented-wave method. *Phys. Rev. B* **50**, 17953–17979 (1994).
- Perdew, J. P. et al. Generalized gradient approximation made simple. *Phys. Rev. Lett.* **77**, 3865–3868 (1996).
- Klimeš, J. et al. Van der Waals density functionals applied to solids. *Phys. Rev. B* **83**, 195131 (2011).

Acknowledgements

This work was financially supported by the National Basic Research Program of China, Fundamental Studies of Perovskite Solar Cells (grant no. 2015CB932200), Natural Science Foundation of China (grants nos. 51602149, 61705102, 61722403 and 11674121), National Key Research and Development Program of China (grants nos. 2017YFA0403403 and 2016YFB0201204), Natural Science Foundation of Jiangsu Province, China (grants nos. BK20161011, BK20161010 and BK20150064), the Young 1000 Talents Global Recruitment Program of China, the Jiangsu Specially Appointed Professor Program, the 'Six talent peaks' Project in Jiangsu Province, China and the Program for JLU Science and Technology Innovative Research Team. Calculations were performed in part at the High Performance Computing Centre of Jilin University.

Author contributions

Y.C. and W.H. conceived and designed the experiments. Y.C. and W.H. supervised the experimental work. L.Z. supervised the theoretical part. H.R. and L.C. carried out the device fabrication and characterizations. Y.Y. and H.D. carried out GIWAXS measurements and analyses. S.Y., Y.S. and L.Z. carried out calculations. S.Z., F.L. and J.Z. carried out XANES measurements. Y.C., H.R., L.Z., S.Y. and Y.X. wrote the first draft of the manuscript. X.G., H.J., J.W. and W.H. participated in data analysis and provided major revisions. All authors discussed the results and commented on the manuscript.

Competing interests

The authors declare no competing interests.

Additional information

Supplementary information is available for this paper at <https://doi.org/10.1038/s41566-019-0572-6>.

Correspondence and requests for materials should be addressed to L.Z., Y.C. or W.H.

Reprints and permissions information is available at www.nature.com/reprints.

Solar Cells Reporting Summary

Nature Research wishes to improve the reproducibility of the work that we publish. This form is intended for publication with all accepted papers reporting the characterization of photovoltaic devices and provides structure for consistency and transparency in reporting. Some list items might not apply to an individual manuscript, but all fields must be completed for clarity.

For further information on Nature Research policies, including our [data availability policy](#), see [Authors & Referees](#).

► Experimental design

Please check: are the following details reported in the manuscript?

1. Dimensions

- Area of the tested solar cells Yes No see Device Characterization in Methods
- Method used to determine the device area Yes No see Device Characterization in Methods

2. Current-voltage characterization

- Current density-voltage (J-V) plots in both forward and backward direction Yes No see Figure 4e
- Voltage scan conditions Yes No see Device Characterization in Methods
For instance: scan direction, speed, dwell times
- Test environment Yes No see Device Characterization in Methods
For instance: characterization temperature, in air or in glove box
- Protocol for preconditioning of the device before its characterization Yes No see Device Characterization in Methods
- Stability of the J-V characteristic Yes No see Stability Characterization in Methods
Verified with time evolution of the maximum power point or with the photocurrent at maximum power point; see ref. 7 for details.

3. Hysteresis or any other unusual behaviour

- Description of the unusual behaviour observed during the characterization Yes No Discuss the J-V hysteresis in Figure 4e and 4f
- Related experimental data Yes No see Figure 4e and 4f

4. Efficiency

- External quantum efficiency (EQE) or incident photons to current efficiency (IPCE) Yes No See Figure S13 in Supplementary Information
- A comparison between the integrated response under the standard reference spectrum and the response measure under the simulator Yes No see Device Characterization in Methods
- For tandem solar cells, the bias illumination and bias voltage used for each subcell Yes No Not relevant to this work.

5. Calibration

- Light source and reference cell or sensor used for the characterization Yes No see Device Characterization in Methods
- Confirmation that the reference cell was calibrated and certified Yes No see Device Characterization in Methods

Calculation of spectral mismatch between the reference cell and the devices under test	<input checked="" type="checkbox"/> Yes <input type="checkbox"/> No	see Device Characterization in Methods
6. Mask/aperture		
Size of the mask/aperture used during testing	<input checked="" type="checkbox"/> Yes <input type="checkbox"/> No	see Device Characterization in Methods
Variation of the measured short-circuit current density with the mask/aperture area	<input type="checkbox"/> Yes <input checked="" type="checkbox"/> No	The mask/aperture area is fixed and cannot change.
7. Performance certification		
Identity of the independent certification laboratory that confirmed the photovoltaic performance	<input checked="" type="checkbox"/> Yes <input type="checkbox"/> No	By an accredited PV Metrology Laboratory of National Institute of Metrology, China
A copy of any certificate(s) <i>Provide in Supplementary Information</i>	<input checked="" type="checkbox"/> Yes <input type="checkbox"/> No	See Figure S10 in Supplementary Information
8. Statistics		
Number of solar cells tested	<input checked="" type="checkbox"/> Yes <input type="checkbox"/> No	60 devices, see Figure 4c
Statistical analysis of the device performance	<input checked="" type="checkbox"/> Yes <input type="checkbox"/> No	see Figure 4c
9. Long-term stability analysis		
Type of analysis, bias conditions and environmental conditions <i>For instance: illumination type, temperature, atmosphere humidity, encapsulation method, preconditioning temperature</i>	<input checked="" type="checkbox"/> Yes <input type="checkbox"/> No	Under ambient atmosphere without any encapsulation at room temperature and 80% (7%) relative humidity, see Figure 5a and 5b; Under continuous heat without any encapsulation at 85 °C in a N2-filled glove box, see Figure 5c and 5d; At maximum power point under AM.1.5G without any encapsulation in a N2-filled glove box, see Figure 5f; Under continuous heat at 85% humidity and 85 °C in air, see Figure S17; Under continuous heat at 150 °C in a N2-filled glovebox, See Figure S18.